ACS Photonics

Article

pubs.acs.org/journal/apchd5

Tunable 3D Plasmonic Cavity Nanosensors for Surface-Enhanced Raman Spectroscopy with Sub-femtomolar Limit of Detection

Mohammadali Tabatabaei,[†] Mohamadreza Najiminaini,[‡,§,∥] Kieffer Davieau,[‡,⊥] Bozena Kaminska,[∥] Mahi R. Singh,[⊥] Jeffrey J. L. Carson,*[,‡,§] and François Lagugné-Labarthet*[,†,⊥]

[†]Department of Chemistry and Center for Advanced Materials and Biomaterials, University of Western Ontario, London, ON N6A 5B7, Canada

[‡]Imaging Program, Lawson Health Research Institute St. Joseph's Health Care, London, ON N6A 4V2, Canada

[§]Department of Medical Biophysics, Schulich School of Medicine and Dentistry, University of Western Ontario, London, ON N6A 5C1, Canada

[∥]The School of Engineering Science, Simon Fraser University, Burnaby, BC V5A 1S6, Canada

[⊥]Department of Physics, University of Western Ontario, London, ON N6A 3K7, Canada

Supporting Information

ABSTRACT: Metallic nanohole arrays (NHAs) with a high hole density have emerged with potential applications for surface-enhanced Raman spectroscopy (SERS) including the detection of analytes at ultralow concentrations. However, these NHA structures generally yield weak localized surface plasmon resonance (LSPR), which is a prerequisite for SERS measurements. In this work, a compact three-dimensional (3D) tunable plasmonic cavity with extraordinary optical transmission properties serves as a molecular sensor with sub-femtomolar detection. The 3D nanosensor consists of a gold film containing an NHA with an underlying cavity and a gold nanocone array at the bottom of the cavity. These nanosensors provide remarkable surface plasmon polariton (SPP) and LSPR coupling, resulting in a significantly improved detection performance. The plasmonic tunability is evaluated both experimentally and theoretically. A SERS limit of detection of 10^{-16} M for 4-nitrothiophenol is obtained along with distribution mapping of the molecule on the 3D plasmonic nanosensor. This results in an improved SERS enhancement factor of 10^7 obtained from a femtoliter plasmonic cavity volume. The tunability of these sensors can give rise to a potential opportunity for use in optical trapping while providing SERS sensing of a molecule of interest.

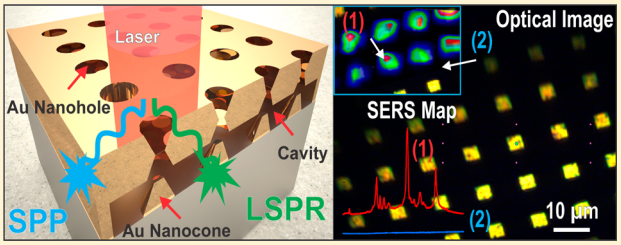

KEYWORDS: *surface-enhanced Raman spectroscopy (SERS), 3D nanosensor, plasmonics, surface plasmon polariton (SPP), localized surface plasmon resonance (LSPR), sub-femtomolar limit of detection*

Molecular plasmonics has shown great promise for trace detection of molecules and biomolecules adsorbed onto rationally designed metallic platforms or particles.[1−4] Among the techniques benefiting from recent advances of plasmon-mediated optical measurements, surface-enhanced Raman spectroscopy (SERS) has pushed the limits for detection of even lower concentrations of analytes. It yields chemical and biological sensing using a variety of surfaces and approaches that mainly relies on the drastic enhancement of the weak Raman signal through the enhancement of the local electromagnetic field in the vicinity of the metallic surface.[5,6] As an analytical technique, SERS provides label-free sensing with high sensitivity and chemical specificity.[7,8] Rational development of SERS platforms includes the production of reproducible engineered metallic platforms with arrays of well-defined structures that combine the functions of (i) trapping the analyte of interest, (ii) improving the sensitivity of the measurement by several orders of magnitude, and (iii) providing quantitative measurements. As the enhancement of electromagnetic fields occurs in nanoscale regions, so-called plasmonic hot spots, integration of specific nanostructures for trapping the interested molecule in these hot spots can improve the sensitivity and reduce the detection time for SERS.[9−13]

Arrays of periodic nanoholes in a metallic film can act as a plasmonic substrate with diverse applications.[14−17] The nanohole array (NHA) structure in an optically thick metal film allows for momentum matching between light incident on an NHA and the surface plasmon (SP) waves existing at the interface between a metal and a dielectric material.[15] The excitation of SPs, so-called surface plasmon polaritons (SPPs), by light incident on a metallic NHA results in extraordinary optical transmission (EOT) and optical resonances. The EOT properties of an NHA depend greatly on material composition and geometrical parameters of the structure.[18−21] Owing to the scattering order of nanoholes, spacing between them and

Received: March 6, 2015
Published: May 4, 2015

DOI: 10.1021/acsphotonics.5b00104
ACS Photonics 2015, 2, 752−759

variable angles of incidence on the NHA, various EOTs related to different SPP modes can be generated at different optical frequencies such as (1, 0) and (1, 1) transmission resonances.[15] NHAs have been widely used in plasmonic applications ranging from optical trapping to sensing of biologically relevant molecules.[20,22−28] For instance, the array acts like a tunable filter since the wavelength selectivity of the array transmission can be adjusted simply by changing the periodicity.[29,30] Many studies have been performed to improve the performance of NHAs for sensing applications. For example, one of the most common applications of NHAs is surface plasmon resonance (SPR) refractive index sensing.[22,25,31] It has been shown that optimal performance can be achieved in SPR sensing for a NHA structure consisting of an ultrasmooth NHA metal surface, elliptical nanohole shapes, and nearly SP energy matching between the top and bottom surfaces of the NHA.[32]

A localized surface plasmon resonance (LSPR) occurs when the incident light interacts with a surface plasmon confined in the vicinity of a metallic nanoparticle, the size of which is comparable to or smaller than the excitation wavelength.[33−35] As a result, the electromagnetic field located in the near-field of the surface is greatly enhanced.[36,37] In this context, the aim is to design a plasmonic structure that will generate a strong LSPR coupling to further enhance the signal of the adsorbed molecule on a 2D or 3D plasmonic nanostructure.[38] Such LSPR plays a pivotal role in many surface-enhanced spectroscopic techniques such as surface-enhanced fluorescence, Raman and infrared spectroscopies, so-called SEF, SERS, and SEIRA, respectively.[33,34,39]

An individual nanohole can produce transmission-based LSPR, which is associated with an interaction of the incident light with an LSPR around the nanohole.[29] Similar properties have been reported for an NHA with enhanced electric field intensity around each nanohole at the corresponding resonance wavelengths.[23] For SERS measurements, NHAs provide typical enhancement factors (EFs) below 10^5, which are weaker than other reliable SERS substrates.[11,12,40] More importantly, these EFs are not reported for very low concentrations of the probe molecules. The reported range is between 2 and 10^4, which is still comparable with some SERS substrates but not likely reliable compared to sensitive SERS substrates with EFs of over 10^5.[8,12,41]

Herein, we evaluated the SERS performance of a 3D metallic nanostructure composed of an array of nanoholes and co-registered nanocones embedded in a single cavity. The optical properties of the nanosensors were investigated experimentally and using optical field modeling. Three major features of these sensors are highlighted in this work: (i) plasmonic tunability; (ii) surface-enhanced Raman spectroscopy of 4-nitrothiophenol (4-NTP) covalently attached on these sensors, and finally (iii) limit of detection of 4-NTP adsorbed onto the sensors with fast acquisition time along with mapping the distribution of the molecules over the platform generating strong signals on the sensors based on the molecular fingerprint.

RESULTS AND DISCUSSION

Physical Characterization of the Fabricated 3D Plasmonic Cavity Nanosensors. Scanning electron microscopy (SEM) images of the nanosensors are shown in Figure 1. These sensors are composed of an NHA membrane with a co-registered nanocone array (NCA). As shown in Figure 1a, this NHA-NCA platform consists of an NHA membrane in a 230 nm thick Au film on a Pyrex substrate with a 250 nm deep cavity, below the surface of the Au film. It can be seen in Figure 1b that at the bottom of the cavity, the co-registered truncated nanocones are aligned with the center of the nanoholes. The schematic representation of 3D plasmonic cavity nanosensors is shown in Figure SI.1a. Demonstrated in Figure 1b, a truncated cone has a height of 150 nm with an apex 100 nm away from the Au film. The hole sizes varied from 74 to 87 nm, and the periodicities varied from 425 to 500 nm with increments of 25 nm. A nanohole consists of two truncated nanocones with their apexes connected at the center of the nanohole. The apex of the cone has a 1:2 ratio with respect to the cone base diameter. For the simulations, the complex refractive indices of Au were provided by Palik, and a refractive index of 1.474 was used for Pyrex.[42]

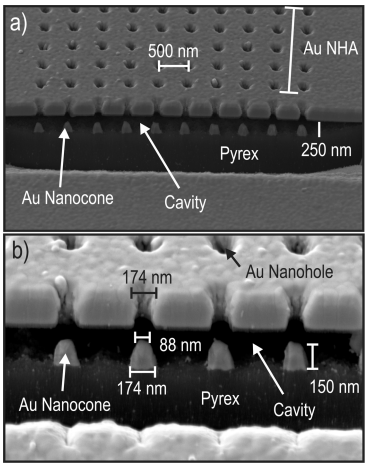

Figure 1. SEM images of 3D plasmonic cavity nanosensors composed of a NHA membrane with co-registered NCA. (a) A 230 nm thick Au NHA membrane with 500 nm periodicity and 87 nm hole radius fabricated on a Pyrex substrate with a single 250 nm deep cavity. (b) Magnified image shown in (a) representing the dimensions of the truncated Au nanocones with an apex radius of 44 nm, a base radius of 87 nm, and a height of 150 nm.

Tunable Cavity 3D Nanosensors. In both simulated and experimentally measured optical transmission spectra of the 3D nanosensors in Figure 2, multiple transmission resonances were observed due to the SPP corresponding to various scattering mode indices. A metallic NHA with a square lattice arrangement of nanoholes results in momentum matching between the in-plane wave vectors of the incident light and the SP, when $\vec{k}_{sp} = (\omega/c)\sin\theta \pm m\vec{u}_x \pm n\vec{u}_y$ is satisfied. The expression $(\omega/c)\sin\theta$ is the in-plane component of the wave vector of the incident light, where ω is the frequency of the incident light, c is the speed of the light, and θ is the incident angle of light.[43] The reciprocal lattice wave vectors $\vec{u}_x$ and $\vec{u}_y$ describe a square lattice when $|\vec{u}_x| = |\vec{u}_y| = (2\pi/a)$, where a is the spacing between adjacent nanoholes and m and n are integers expressing the scattering mode indices. From the conservation of energy, the SP dispersion relationship on a smooth metal surface can be expressed as $|\vec{k}_{sp}| = |\vec{k}_0|[\varepsilon_m\varepsilon_d/(\varepsilon_m + \varepsilon_d)]^{1/2}$, where ε_d and ε_m are the dielectric functions of the incident medium (at the top or bottom surface of the nanohole) and the metal film. By combining the momentum-matching condition of the light-SP for light at normal incidence to the NHA and the dispersion relation of the SP, the EOT positions of an NHA associated with the SPP can be expressed by eq 1:

DOI: 10.1021/acsphotonics.5b00104
ACS Photonics 2015, 2, 752−759

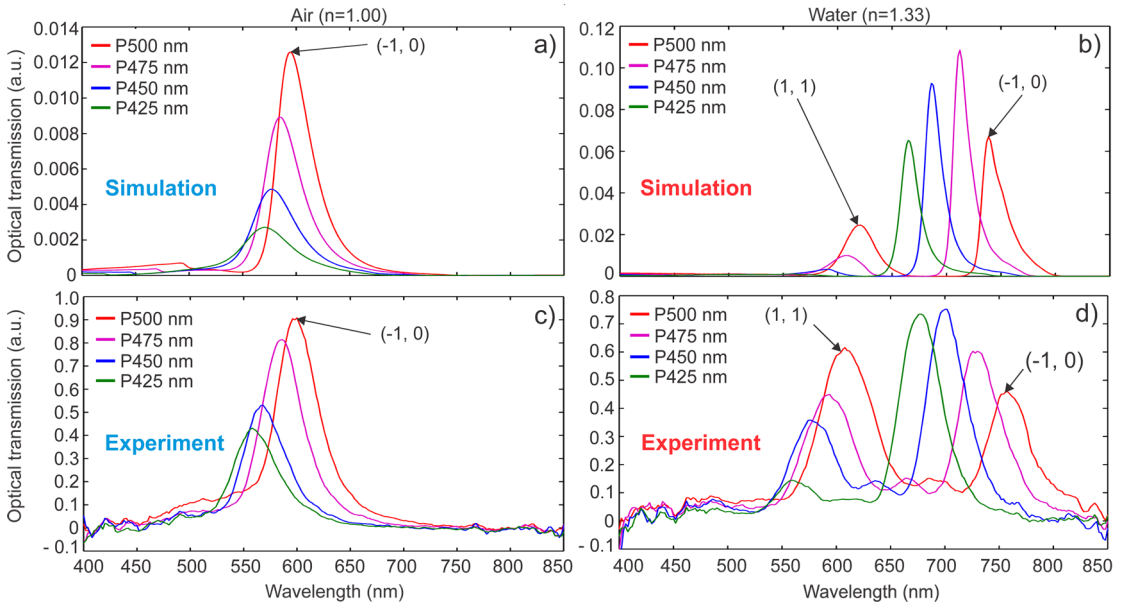

Figure 2. Optical transmission spectra of 3D plasmonic nanosensors for simulated and experimental results. The periodicities range from 425 nm (green curve) to 500 nm (red curve) with increments of 25 nm. Simulated results for (a) air (n = 1.00) and (b) water (n = 1.33); experimental results for (c) air (n = 1.00) and (d) water (n = 1.33).

$$\lambda_{max} \cong \frac{a}{\sqrt{m^2 + n^2}} \sqrt{\frac{\varepsilon_m \varepsilon_d}{\varepsilon_m + \varepsilon_d}} \quad (1)$$

The simulated and experimentally measured optical transmission spectra of the platforms for various periodicities are shown in Figure 2 for platforms surrounded by air (n = 1.00) or immersed in water (n = 1.33). When the structures are in air, both simulation and experimental results showed a single transmission resonance, which can be associated with the (−1, 0) excitation of the SP on the top and bottom surface of the NHA membrane. However, this resonance has been also induced with the presence of a truncated nanocone at the bottom of the cavity. The apex of the truncated nanocone and the bottom of the nanohole would generate a nanoantenna effect at the resonance wavelength, which would generate a localized SP between two aforementioned nanosensors. As a result, the (−1, 0) resonance is related to not only SPPs but also LSPRs. As the periodicity of the hole decreases, the resonance transmission of the 3D nanosensors are blue-shifted to shorter wavelengths (Figure 2a and c). The existence of LSPR coupling was observed between the nanocone and nanohole in the simulation model, which resulted in generation of an antenna and strong hot spot within this area. Although a nanocone structure without the presence of a nanohole could have two LSPRs located at the base and at the apex, the combination of both structures yields a strong local coupling of the respective LSPRs. The presence of a nanocone alters both the resonance frequency of the LSPRs and the transmission efficiency of a NHA due to the shadowing effect and optical absorption of the nanocone.[23] However, an NHA without nanocones cannot generate a strong LSPR similar to the proposed structure and would have more limited detection and sensitivity in the SERS applications according to the previous studies on NHAs.[11,12,40]

Due to the bulk plasmon wavelength of Au at 500 nm, the resonance of the 3D nanosensors decays for smaller periodicity as the resonance blue-shifts toward 500 nm. When the 3D nanostructure is encapsulated in water, the LSPR-SPP-mediated resonances of the 3D nanosensors are red-shifted toward longer wavelengths (Figure 2b and d). Two LSPR-SPP resonances were seen in the optical transmission spectra of the 3D nanosensors. The resonances were associated with (−1, 0) and (1, 1) scattering hole orders of the 3D nanosensors. The electric field intensity of 3D nanosensors with 500 nm periodicty is shown in Figure 3 at the LSPR-SPP resonance

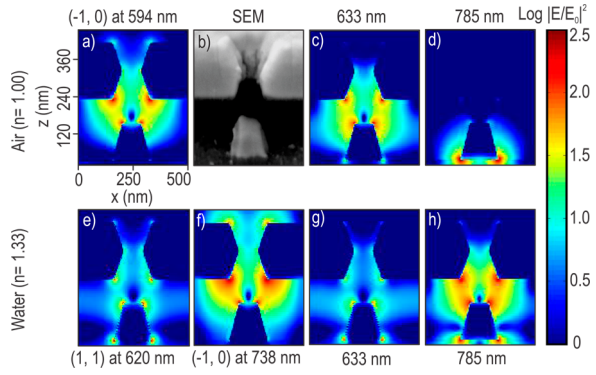

Figure 3. Electric field ($|E/E_0|^2$, log scale representation) intensity of a unit cell in a 3D plasmonic nanosensor displayed on the xz plane. The electric field intensity for air (n = 1.00) at the (−1, 0) peak at (a) 594 nm, (c) 633 nm, and (d) 780 nm. The SEM image of the actual structure of represented simulated images is shown in (b). The electric field intensity for water (n = 1.33) at (e) the (1, 1) peak at 620 nm and (f) the (−1,0) peak at 738 nm, (g) 633 nm, and (h) 785 nm.

wavelengths of 633 and 785 nm for both air and water surrounding media. The electric field distributions at LSPR-SPP resonances for air and water confirm that there is a strong LSPR coupling between the bottom of the hole and the apex of the nanocone. This structure generates the highest electric field at the resonance peak. However, the electric field at the (1, 1) LSPR-SPP resonance is of weaker intensity compared to the electric field at (−1, 0) resonance. The electric field at 633 nm appeared to be more intense in air, whereas it was lower when

DOI: 10.1021/acsphotonics.5b00104
ACS Photonics 2015, 2, 752−759

the platform was immersed in water. This was due to the presence of the (−1, 0) resonance peak close to 633 nm for a 3D nanosensor with 500 nm periodicity located in air. In contrast, the electric field at 785 nm was significantly higher within the apex of the truncated cone and the bottom surface of the hole compared to that obtained in air at 785 nm. There was a high absorption at the base of the truncated nanocone due to the LSPR absorption properties of the 3D nanosensor. Similar results are expected when the platform is immersed in a polar organic solvent such as ethanol (n = 1.36) based on its simulated optical transmission shown in Figure SI2.

Effect of Plasmonic Tunability on SERS. As shown in Figure 4, the SERS spectra of the 4-NTP molecules (1 mM)

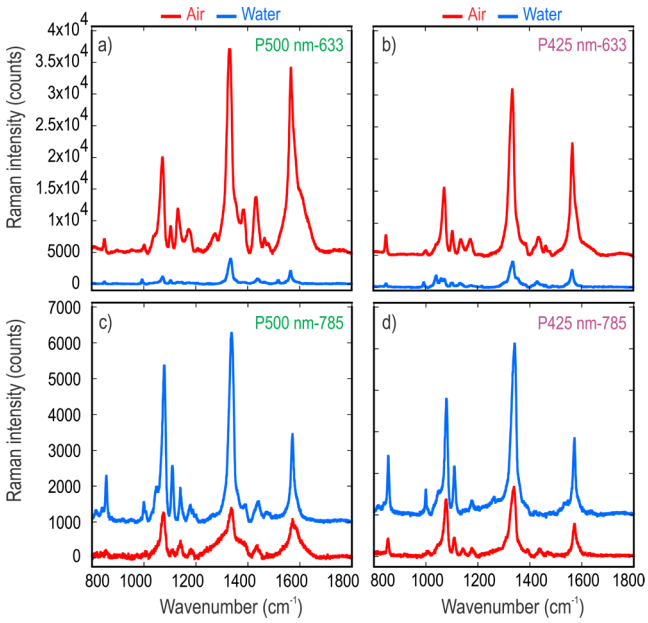

Figure 4. SERS spectra of 4-NTP adsorbed on the 3D nanosensors with different periodicities, medium (air and water), and wavelength of incident light. (a) P500 nm and (b) P425 nm periodicities at 633 nm incident light in air (red) and water (blue); (c) P500 nm and (d) P425 nm periodicities at 785 nm in air (red) and water (blue). Acquisition time for each spectrum was 3 s with five accumulations. Base line correction was applied to all spectra. A +5000 counts offset was applied to both red spectra in (a) and (b). A +1000 counts offset was applied to both blue spectra in (c) and (d). These offsets were applied to represent the data in a more comparable fashion.

were collected on different 3D nanosensors in two different media (air and water) and also for two wavelengths of incident light (633 and 785 nm). Using the 633 nm laser, the SERS signals of 4-NTP integrated for the ν_s NO_2 mode (1337 cm^{-1}) were stronger for 3D nanosensors with periodicities of 500 (3.2×10^4 counts) and 425 nm (2.5×10^4 counts) when the signal was collected in air compared to water (Figure 4a and b). When the 785 nm laser was used, the SERS intensities of 4-NTP were stronger for both 3D nanosensors, P500 (5.4×10^3 counts) and P425 (4.1×10^3 counts), when collected in water compared to air (Figure 4c and d). These phenomena are also related to the tuned plasmonic bands of the 3D nanosensors in air and water as shown in Figure 2. We observed similar responses for 3D nanosensors with periodicities of 475 and 450 nm (Figure SI3). We also observed a decrease in the 4-NTP SERS signal when the periodicity was decreased from 500 to 425 nm, which was related to the dependence of the plasmonic bands on periodicity. For instance, from 500 to 425 nm, the plasmonic band is blue-shifted to wavelengths below 600 nm in both simulations and experiment (Figure 2a and c).

SERS Mapping of Hot Spots on 3D Plasmonic Nanosensors. In order to evaluate the detection limit of our 3D nanosensors, platforms were functionalized with a 100 attomolar (aM) solution of the 4-NTP. The transmission optical image of the array of P500 3D nanosensors is shown in Figure 5a. The SERS mapping was performed on the selected

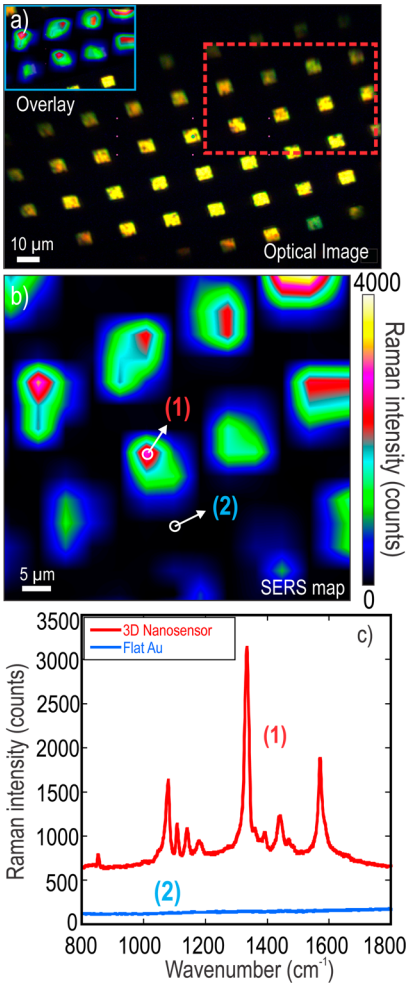

Figure 5. Surface-enhanced Raman mapping of 4-NTP adsorbed on the 3D nanosensors with 500 nm periodicity in air with 633 nm incident light. Acquisition time for each spectrum was 1 s with a 1 μm step size. (a) Transmission optical image of 3D nanosensors with overlaid SERS mapping (inset) for the area outlined with a red dashed box. (b) Raman mapping of the outlined area in panel (a). (c) Spectra of the regions marked (1) and (2) in panel (b). No baseline correction was applied to spectra in panel (c).

area in red shown in Figure 5a. The map was generated by integrating the intensity of the stretching mode of the nitro group (νs NO_2) in the 1282−1400 cm^{-1} spectral range. A strong SERS intensity (bright regions) corresponded to the location of the 3D nanosensors and, therefore, the location of the hot spots. This is the case for spot 1 in Figure 5b. However, regions away from the 3D nanosensors (labeled spot 2 in Figure 5b) show a considerably weaker SERS signal. This lack of enhancement was attributed to positions containing only flat Au. As shown in the inset of Figure 5a, the relationship between

DOI: 10.1021/acsphotonics.5b00104
ACS Photonics 2015, 2, 752−759

the location of the 3D nanosensors in the optical image and the locations of strong SERS intensity was maintained. As a result, the detection of 4-NTP drop-casted onto the 3D nanosensors was possible even at a concentration of 100 aM and with a rapid acquisition time of 1 s. The distinguishable locations of the 3D nanosensors based on the Raman map proved the reproducible ability of the sensors to generate a strong signal for low concentrations of molecules trapped in the nanoscale hot spots. Noteworthy, as stated previously, the engineered 3D nanosensors allow for coupling of SPP and LSPR, which generates strong hot spots between nanoholes and nanocones. Furthermore, the 3D structure of nanosensors potentially increases the surface area for attachment of probe molecules to the surface of the nanostructure compared to a planar structure. This effect has been observed in other studies for SERS substrates compared to a 2D array of nanosensors.[38] For instance, in this case, the 3D nanosensors have surface areas on both top and bottom surfaces of a gold NHA membrane as well as on the nanocone itself compared to the planar NHA structure.

Limit of Detection for 3D Nanosensors. In order to evaluate the limit of detection of such cavity-based sensors, the platforms were functionalized with 4-NTP at concentrations between 1 μM and 1aM. In order to avoid cross contamination between high and low concentration experiments, each SERS experiment was repeated 3−5 times onto freshly prepared arrays of 3D nanosensors (P500−P425). Furthermore, the experiments were conducted for an average of 10−15 spots on each platform. Figure 6a shows that all the main peaks of the 4-NTP were detectable between 1 μM and 100 aM.[44] However, we observed a small but measurable change in the intensity of the SERS signal for 1aM 4-NTP, even though at this concentration it was statistically unlikely to find a spot with a single or a few molecules trapped in the plasmonic cavity of the 3D nanosensors. Compared to higher concentrations of 4-NTP, there were fewer spots on the 3D nanosensors that provided a SERS signal, and the signals were not stable over long exposures. In most of the 2D plasmonic substrates for SERS, providing a reproducible global signal requires at least a homogeneous monolayer of the probe molecule attached onto the surface.[38] The advantage of nanostructures with an embedded cavity can be highlighted here, as they provide a better opportunity to trap the molecule in the nanoscale hot spots compared to equivalent 2D structures. A reliable Raman signal collected from these 3D nanosensors was obtained for concentrations down to 100 aM. This can be clearly observed by evaluating the intensity of the main peak of NO_2 (Figure 6a inset). Comparing the signal at 100 and 1 aM, it is apparent that the signal has mostly vanished for 1 aM. These measurements yield a limit of detection of ∼100 aM (Figure 6a).

Due to the fact that altering the conditions of the experiment plays a key role in obtaining the SERS signal for different structures, the measurements for 100 aM 4-NTP were repeated with microscope objectives of different numerical apertures (N.A.). Increasing the N.A. of the objective resulted in an enhanced SERS signal (compare the main peak of NO_2 in Figure 6b). The SERS signals were enhanced almost 2 times when increasing the N.A. from 0.5 to 0.75 and 3 times when increasing the N.A. up to 0.9.

By increasing the N.A. of the microscope objective, the laser beam was more confined at the apex of the nanocone and the bottom of the nanohole, resulting in a more efficient hot spot

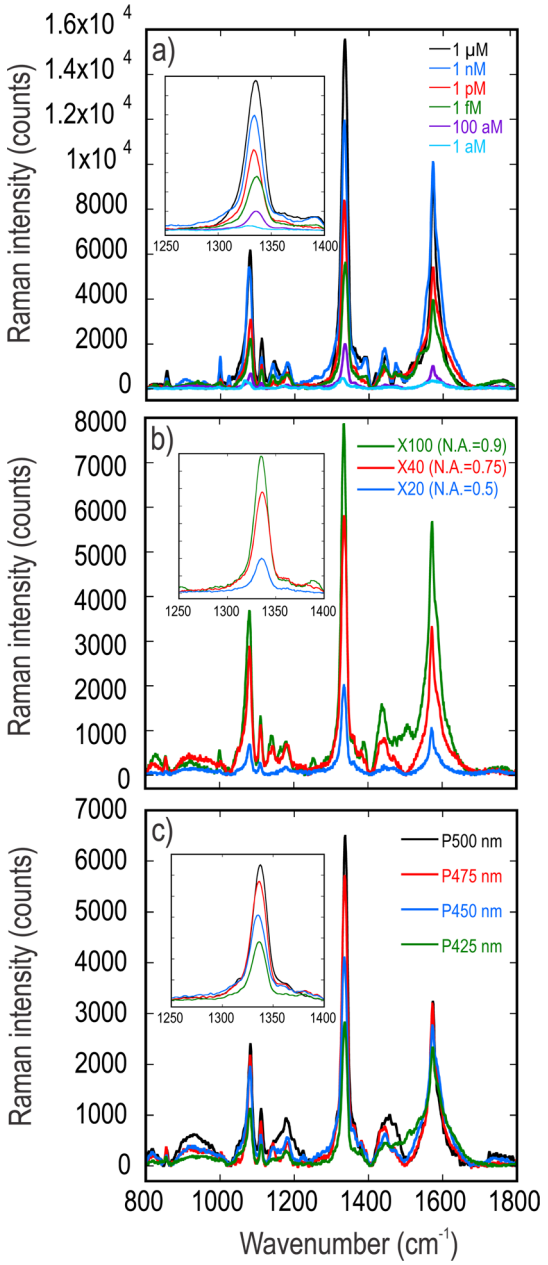

Figure 6. SERS spectra of 4-NTP adsorbed onto 3D nanosensors collected by using a 633 nm incident laser in air. (a) Different concentrations (1 aM to 1 mM) of 4-NTP adsorbed on the 3D nanosensors with 500 nm periodicity. (b) The effect of numerical aperture and magnification on SERS spectra of 100 aM 4-NTP absorbed on the 3D nanosensors. (c) SERS spectra of 100 aM 4-NTP adsorbed on the 3D nanosensors. Baseline correction was applied to all spectra. SERS signals of the main NO_2 peak are shown within each inset in each panel.

and LSPR. It can also be beneficial to decrease the laser spot even further to be more focused on the 3D nanosensors, thereby excluding the scattering from flat Au regions around the hot spots. To evaluate the sensitivity of different 3D nanosensors based on their periodicities, the SERS signals have been collected with the same concentration of 100 aM. As shown in Figure 6c, a decreasing trend was observed for the SERS signal when the periodicity of the platforms was decreased from 500 nm to 425 nm. These results have a similar trend to measurements performed with 1 mM 4-NTP.

DOI: 10.1021/acsphotonics.5b00104
ACS Photonics 2015, 2, 752−759

This trend was clearly observed, as shown in the inset of Figure 6c.

Estimation of a SERS Enhancement Factor. Generally speaking, the definition of the SERS EF can be considered as the ratio between the SERS intensity per adsorbed molecule and the normal Raman intensity per bulk molecule. However, in SERS, the EF for a given molecule varies with the opto-geometric conditions of the SERS measurement and corresponding reference measurement.[45] The determination of the number of molecules that yield the Raman signal and their contribution to the EF is not trivial and may lead to erroneous estimations. The ensemble of parameters that need to be considered when performing a SERS experiment, such as probing a single molecule or multiple molecules, the orientation of the molecules in the experimental system, the spatial distribution, or the experimental limitations in resolution, can be used only to approximate an EF.

The Raman signal is enhanced through both the excitation and the emission processes, as shown in eq 2:[46]

$$F = |(E_{\nu_{\text{excitation}}})|^2 |(E_{\nu_{\text{Raman}}})|^2 \tag{2}$$

where $E(\nu_{\text{excitation}})$ and $E(\nu_{\text{Raman}})$ are the local electric-field EFs at the incident frequency ($\nu_{\text{excitation}}$) and at the Raman Stokes frequency (ν_{Raman}), respectively. However, since the plasmon frequency width is large compared to the Raman Stokes shift, both electromagnetic fields are often in resonance and/or preresonance with the plasmon band. Therefore, an approximation is to assume that $E(\nu_{\text{excitation}})$ and $E(\nu_{\text{Raman}})$ are the same, leading to an EF proportional to $F = |E(\nu_{\text{excitation}})|^4$. In such an approximation, the matching of the excitation laser line with the plasmon frequency is an essential condition to obtain large Raman surface enhancements. In order to establish the relationship between the nanostructured surface and the SERS activity of the platform, the EFs have been determined. The determination of the EF in SERS is a prerequisite to quantify the enhancement of the Raman signal. The surface Raman EF can be estimated by comparing the measured SERS intensities (I_{SERS}) with the nonenhanced Raman scattering intensities (I_{NE}) as shown in eq 3:[47,48]

$$\text{EF} = \frac{N_{\text{NE}} \times I_{\text{SERS}}}{I_{\text{NE}} \times N_{\text{SERS}}} = 1.2 \times 10^7 \tag{3}$$

The EF obtained in eq 3 is calculated based on the number of molecules that are statistically located in the confocal excitation volume and their associated SERS signals. The Raman intensity of the main peak of 4-NTP, the stretching mode of the nitro group (νs NO_2), was used as the reference peak for these calculations. Further details regarding the approximations and calculations can be found in the SI. Such EF obtained for a 100 aM solution in a femtoliter plasmonic cavity represents the promising chemical sensitivity of these 3D nanosensors (Figure SI5). For 100 aM concentration, there are about two or three molecules within the focal spot. Noteworthy, about four nanostructures are located within the same area. Therefore, to obtain a SERS signal, the molecules should be adsorbed within these hot spots. In our experiments performed with 100 aM concentration, most of our measurements have shown SERS activity as opposed to lower concentrations (1 aM). However, some individual nanostructures appeared to be SERS inactive presumably due to the absence of the probe molecules or structural defects.

CONCLUSIONS

In this work, for the first time, the capability of cavity-based plasmonic nanosensors is demonstrated for SERS-based molecular sensing. These nanosensors provide extraordinary optical transmission properties, which can generate strong SPP and LSPR coupling. These phenomena have been shown here by simulated and experimental optical transmission measurements. The experimental results were also in good agreement with the FDTD calculations for electromagnetic field distributions at the plasmonic bands of the nanosensors. In the meantime, these structures represent a plasmonic tunability with respect to the media of the experiment and also the wavelength of the incident light. These 3D nanosensors also provide a remarkable molecular limit of detection of 10^{-16} M for a probe molecule (4-NTP) with a short acquisition time of 1 s. Consequently, a reliable EF of $\sim 10^7$ is achieved for these sensors for an extremely low concentration of 100 aM from a femtoliter plasmonic probe volume. Reproducible SERS signals have been collected on the 3D nanosensors with concentrations down to 100 aM, providing the spatial distribution of hot spots on the plasmonic substrate. It is also shown that by increasing the N.A. of the objectives, an enhancement occurs for the SERS signals obtained on these sensors, proving the confined strong LSPR coupling in the NHA-NCA interface. The strong LSPR coupling of these nanosensors can introduce them to other spectroscopic techniques such as SEF, SEIRA, and even tip-enhanced Raman spectroscopy (TERS), in which there is better control over the polarization of light. Of even greater interest, the plasmonic tunability of these sensors can be used for simultaneous optical trapping and surface-enhanced detection.

METHODS

Fabrication of 3D Plasmonic Cavity Nanosensors. The plasmonic cavities were fabricated using electron beam lithography (EBL) methodology. First, electron-beam physical vapor deposition (EB-PVD) was used to deposit a 3 nm thin Ti layer on a Pyrex substrate. This ensured that the substrate surface was conductive for the EBL writing process. A 500 nm thick layer of photoresist (negative tone photoresist ma-N 2403) was then spin-coated onto the Ti layer and soft baked at 90 °C for 60 s. The sample was placed into an EBL machine (LEO, 1530 e-beam lithography), where the nanohole array patterns were written on the photoresist layer. The sample was developed in MF 319 developer (Shipley, Marlborough, MA, USA) for 40 s, leaving behind photoresist nanopillars, which acted as a mask to create the nanoholes in the metal film. Another 3 nm thick Ti layer was deposited to create an adhesion layer followed by 80 nm deposition of Au using an EB-PVD deposition instrument. Once the Au layer was deposited, the sample was left in PG Remover solution at 80 °C to lift off the photoresist nanopillars and leave behind the NHAs in the Au film. Once the NHAs were created, a TFT Ti etchant (Transene Company, Inc.) was used to etch away both the Ti layer and Pyrex, forming a large cavity beneath the gold NHA. The sample was in Ti etchant for 70 s and resulted in a 250 nm deep cavity. Afterward, 150 nm Au was deposited onto the structure to create a truncated nanocone beneath each nanohole on the bottom surface of the cavity. The SEM images of the fabricated 3D plasmonic nanosensors with 500 nm periodicy are shown in Figure 1. The presence of the 250 nm deep cavity and 150 nm tall truncated NCA beneath the NHA membrane structure is shown in these SEM images. Each 3D

DOI: 10.1021/acsphotonics.5b00104
ACS Photonics 2015, 2, 752−759

nanosensor had dimensions of approximately 5 μm by 5 μm and was repeated in a 7 by 7 square lattice arrangement with a periodicity of 10 μm. In order to clean the platform for further use, O_2 plasma and UV-O_3 exposure are efficient methods. The substrate can also be cleaned by Nanostrip (90% sulfuric acid, 5% peroxymonosulfuric acid, <1% hydrogen peroxide, and 5% water) to remove all the impurities and subsequently washed with ultrapure Milli-Q water and dried under nitrogen prior to O_2 or UV-O_3 cleaning.

Numerical Simulation of 3D Plasmonic Cavity Nanosensors. Modeling of the electromagnetic field was performed using the finite-difference time-domain (FDTD) method to numerically solve Maxwell's equations (FDTD Solutions, Lumerical Inc., Vancouver, Canada). As shown in Figure SI.1b, FDTD calculations were performed by creating a 3D unit cell that was simulated with periodic boundary conditions on the *x*- and *y*-axes, and a perfectly matched layer (PML) boundary condition on the *z*-axis. A rectangular, Cartesian-style mesh was placed around the unit cell with a maximum mesh setting of 3 nm. The mesh settings can be altered to increase the accuracy of the simulation by increasing the number of points within the mesh.

Optical Characterization Setup. The optical transmission spectra of the platforms were measured, using an inverted microscope (Nikon, TE300) attached to a photometer (PTI, D104), monochromator (PTI, 101), and a photomultiplier (PTI, 710). A 100 W halogen lamp produced unpolarized white light, which was focused onto the structure using a bright-field condenser lens (N.A. = 0.3) on the microscope. A 20× objective (N.A. = 0.45; Nikon, 93150) was used to collect the scattered light, which was then guided to the photometer using a beam splitter. Light from a desired region on the sample was selected by adjusting the apertures on the photometer. The light from this desired region was then guided to the monochromator for spectral analysis. The optical transmission spectra were corrected for the background intensity (dark noise) and normalized by the intensity of the light source.

SERS Measurements and Sample Preparation. The Raman measurements were performed using a Horiba Jobin-Yvon Raman spectrometer equipped with a 600 g/mm grating and a 632.8 or 785 nm excitation with proper interference and edge filters. For both laser sources, intensities were set to 2 mW or 200 μW at the sample using neutral density filters with 1.0 or 2.0 optical densities, respectively. Olympus microscope objectives of 20× (N.A.= 0.5), 40× (N.A.= 0.75), and 100× (N.A.= 0.9) were used for all experiments. The pinhole of the spectrometer was opened to 200 μm. All of the Raman spectra collected for individual spots were the result of 3 s exposures, while the maps were the result of 1 s exposures. The maps were integrated within 1316 to 1354 cm^{-1}. A stock solution of 4-NTP (10^{-3} M) in ethanol was made. This stock solution was then further diluted to yield 2 mL of solutions with concentrations ranging from 10^{-6} to 10^{-18} M. Two drops of the as-prepared solution (~100 μL) were deposited onto one platform and then placed into a Petri dish. All glassware used for functionalization and washing were new to avoid contamination. The Petri dish was sealed and stored in the refrigerator for the duration of the functionalization. For the determination of limit of detection, the platforms were functionalized overnight (24 h). Each platform was then washed into a beaker of ethanol (99.9%) three times to remove any excess 4-NTP not adsorbed onto the surface. The platforms were then dried under nitrogen. Each SERS measurement was performed 3−5 times. The spectra of 10−15 spots were collected on each 3D nanosensor, and the average value of the intensities was used in all relevant graphs (Figure SI4).

■ ASSOCIATED CONTENT

Supporting Information

Layout of FDTD simulation and schematic representation of the 3D nanosensors, SERS signals of P475, and P450 for 1 mM 4-NTP with different conditions, simulated optical transmission spectra of 3D cavity plasmonic nanosensors in ethanol, detailed EF calculations, and standard error analysis of SERS signals are shown. The Supporting Information is available free of charge on the ACS Publications website at DOI: 10.1021/acsphotonics.5b00104.

■ AUTHOR INFORMATION

Corresponding Authors

*E-mail: jcarson@lawsonimaging.ca (J. J. L. Carson).
*E-mail: flagugne@uwo.ca (F. Lagugné-Labarthet).

Notes

The authors declare no competing financial interest.

■ ACKNOWLEDGMENTS

The authors wish to gratefully acknowledge the Center for Advanced Material and Biomaterial for supporting the work done in the Nanofabrication Facility at the University of Western Ontario. This research was funded by Natural Sciences and Engineering Research Council of Canada (NSERC) Discovery Grants (F.L.-L., J.J.L.C., B.K.) and by the Canada Research Chairs program (F.L.-L., B.K.). Dr. Mohamadreza Najiminaini was partially supported by the MITACS program.

■ REFERENCES

(1) Brolo, A. G. Plasmonics for future biosensors. *Nat. Photonics* **2012**, *6*, 709−713.
(2) Passarelli, N.; Pérez, L. A.; Coronado, E. A. Plasmonic interactions: from molecular plasmonics and Fano resonances to ferroplasmons. *ACS Nano* **2014**, *8*, 9723−9728.
(3) Sonntag, M. D.; Klingsporn, J. M.; Zrimsek, A. B.; Sharma, B.; Ruvuna, L. K.; Van Duyne, R. P. Molecular plasmonics for nanoscale spectroscopy. *Chem. Soc. Rev.* **2014**, *43*, 1230−1247.
(4) Baffou, G.; Quidant, R. Nanoplasmonics for chemistry. *Chem. Soc. Rev.* **2014**, *43*, 3898−3907.
(5) Fleischmann, M.; Hendra, P. J.; McQuillan, A. J. Raman spectra of pyridine adsorbed at a silver electrode. *J. Chem. Phys. Lett.* **1974**, *26*, 163−166.
(6) Jeanmaire, D. L.; Van Duyne, R. P. Surface Raman spectroelectrochemistry: Part I. Heterocyclic, aromatic, and aliphatic amines adsorbed on the anodized silver electrode. *J. Electroanal. Chem.* **19977**, *84*, 1−20.
(7) Nie, S.; Emory, S. R. Probing single molecules and single nanoparticles by surface-enhanced Raman scattering. *Science* **1997**, *275*, 1102−1106.
(8) Kneipp, K.; Wang, Y.; Kneipp, H.; Perelman, L. T.; Itzkan, I.; Dasari, R. R.; Feld, M. S. Single molecule detection using surface-enhanced Raman scattering (SERS). *Phys. Rev. Lett.* **1997**, *78*, 1667−1670.
(9) Sheehan, P. E.; Whitman, L. J. Detection limits for nanoscale biosensors. *Nano Lett.* **2005**, *5*, 803−807.
(10) Squires, T. M.; Messinger, R. J.; Manalis, S. R. Making it stick: convection, reaction and diffusion in surface-based biosensors. *Nat. Biotechnol.* **2008**, *26*, 417−426.
(11) Kumar, S.; Cherukulappurath, S.; Johnson, T. W.; Oh, S.-H. Millimeter-sized suspended plasmonic nanohole arrays for surface-

DOI: 10.1021/acsphotonics.5b00104
ACS Photonics 2015, 2, 752−759

tension-driven flow-through SERS. *Chem. Mater.* **2014**, *26*, 6523−6530.
(12) Brolo, A. G.; Arctander, E.; Gordon, R.; Leathem, B.; Kavanagh, K. L. Nanohole-enhanced Raman scattering. *Nano Lett.* **2004**, *4*, 2015−2018.
(13) Im, H.; Sutherland, J. N.; Maynard, J. A.; Oh, S.-H. Nanohole-based surface plasmon resonance instruments with improved spectral resolution quantify a broad range of antibody-ligand binding kinetics. *Anal. Chem.* **2012**, *84*, 1941−1947.
(14) Barnes, W. L.; Dereux, A.; Ebbesen, T. W. Surface plasmon subwavelength optics. *Nature* **2003**, *424*, 824−830.
(15) Ebbesen, T. W.; Lezec, H. J.; Ghaemi, H. F.; Thio, T.; Wolff, P. A. Extraordinary optical transmission through sub-wavelength hole arrays. *Nature* **1998**, *391*, 667−669.
(16) Valsecchi, C.; Brolo, A. G. Periodic metallic nanostructures as plasmonic chemical sensors. *Langmuir* **2013**, *29*, 5638−5649.
(17) Lee, M.; Kim, J.; Seo, W.; Hong, H.-G.; Song, Y.; Dasari, R. R.; An, K. Three-dimensional imaging of cavity vacuum with single atoms localized by a nanohole array. *Nat. Commun.* **2014**, *5*, 3441.
(18) Krishnan, A.; Thio, T.; Kim, T. J.; Lezec, H. J.; Ebbesen, T. W.; Wolff, P. A.; Pendry, J.; Martin-Moreno, L.; Garcia-Vidal, F. J. Evanescently coupled resonance in surface plasmon enhanced transmission. *Opt. Commun.* **2001**, *200*, 1−7.
(19) Najiminaini, M.; Vasefi, F.; Kaminska, B.; Carson, J. J. L. Effect of surface plasmon energy matching on the sensing capability of metallic nano-hole arrays. *Appl. Phys. Lett.* **2012**, *100*, 063110.
(20) Najiminaini, M.; Vasefi, F.; Kaminska, B.; Carson, J. J. L. Nano-hole array structure with improved surface plasmon energy matching characteristics. *Appl. Phys. Lett.* **2012**, *100*, 043105.
(21) Przybilla, F.; Degiron, A.; Laluet, J.-Y.; Genet, C.; Ebbesen, T. W. Optical transmission in perforated noble and transition metal films. *J. Opt. A: Pure Appl. Opt.* **2006**, *8*, 458.
(22) Brolo, A. G.; Gordon, R.; Leathem, B.; Kavanagh, K. L. Surface plasmon sensor based on the enhanced light transmission through arrays of nanoholes in gold films. *Langmuir* **2004**, *20*, 4813−4815.
(23) Najiminaini, M.; Ertorer, E.; Kaminska, B.; Mittler, S.; Carson, J. J. L. Surface plasmon resonance sensing properties of a 3D nanostructure consisting of aligned nanohole and nanocone arrays. *Analyst* **2014**, *139*, 1876−1882.
(24) Gordon, R.; Sinton, D.; Kavanagh, K. L.; Brolo, A. G. A new generation of sensors based on extraordinary optical transmission. *Acc. Chem. Res.* **2008**, *41*, 1049−1057.
(25) Im, H.; Wittenberg, N. J.; Lesuffleur, A.; Lindquist, N. C.; Oh, S.-H. Membrane protein biosensing with plasmonic nanopore arrays and pore-spanning lipid membranes. *Chem. Sci.* **2010**, *1*, 688−696.
(26) Im, H.; Lee, S. H.; Wittenberg, N. J.; Johnson, T. W.; Lindquist, N. C.; Nagpal, P.; Norris, D. J.; Oh, S.-H. Template-stripped smooth Ag nanohole arrays with silica shells for surface plasmon resonance biosensing. *ACS Nano* **2011**, *5*, 6244−6253.
(27) Wang, Y.; Kar, A.; Paterson, A.; Kourentzi, K.; Le, H.; Ruchhoeft, P.; Willson, R.; Bao, J. Transmissive nanohole arrays for massively-parallel optical biosensing. *ACS Photonics* **2014**, *1*, 241−245.
(28) Ricciardi, A.; Consales, M.; Quero, G.; Crescitelli, A.; Esposito, E.; Cusano, A. Versatile optical fiber nanoprobes: from plasmonic biosensors to polarization-sensitive devices. *ACS Photonics* **2014**, *1*, 69−78.
(29) Genet, C.; Ebbesen, T. W. Light in tiny holes. *Nature* **2007**, *445*, 39−46.
(30) Yokogawa, S.; Burgos, S. P.; Atwater, H. A. Plasmonic color filters for CMOS image sensor applications. *Nano Lett.* **2012**, *12*, 4349−4354.
(31) Yanik, A. A.; Cetin, A. E.; Huang, M.; Artar, A.; Mousavi, S. H.; Khanikaev, A.; Connor, J. H.; Shvets, G.; Altug, H. Seeing protein monolayers with naked eye through plasmonic Fano resonances. *Proc. Nat. Acad. Sci.* **2011**, *108*, 11784−11789.
(32) Cervantes Tellez, G. A.; Hassan, S. a.; Tait, R. N.; Berini, P.; Gordon, R. Atomically flat symmetric elliptical nanohole arrays in a gold film for ultrasensitive refractive index sensing. *Lab Chip* **2013**, *13*, 2541−2546.
(33) Fayyaz, S.; Tabatabaei, M.; Hou, R.; Lagugné-Labarthet, F. Surface-enhanced fluorescence: mapping individual hot spots in silica-protected 2D gold nanotriangle arrays. *J. Phys. Chem. C* **2012**, *116*, 11665−11670.
(34) Aroca, R. F.; Ross, D. J.; Domingo, C. Surface-enhanced infrared spectroscopy. *Appl. Spectrosc.* **2004**, *58*, 324A−338A.
(35) Jensen, T.; Kelly, L.; Lazarides, A.; Schatz, G. Electrodynamics of noble metal nanoparticles and nanoparticle clusters. *J. Cluster Sci.* **1999**, *10*, 295−317.
(36) Merlen, A.; Lagugné-Labarthet, F. Imaging the optical near field in plasmonic nanostructures. *Appl. Spectrosc.* **2014**, *68*, 1307−1326.
(37) Bukasov, R.; Ali, T. A.; Nordlander, P.; Shumaker-Parry, J. S. Probing the plasmonic near-field of gold nanocrescent antennas. *ACS Nano* **2010**, *4*, 6639−6650.
(38) Tabatabaei, M.; Sangar, A.; Kazemi-Zanjani, N.; Torchio, P.; Merlen, A.; Lagugné-Labarthet, F. Optical properties of silver and gold tetrahedral nanopyramid arrays prepared by nanosphere lithography. *J. Phys. Chem. C* **2013**, *117*, 14778−14786.
(39) Brown, L. V.; Yang, X.; Zhao, K.; Zheng, B. Y.; Nordlander, P.; Halas, N. J. Fan-shaped gold nanoantennas above reflective substrates for surface-enhanced infrared absorption (SEIRA). *Nano Lett.* **2015**, *15*, 1272−1280.
(40) Yu, Q.; Guan, P.; Qin, D.; Golden, G.; Wallace, P. M. Inverted size-dependence of surface-enhanced Raman scattering on gold nanohole and nanodisk arrays. *Nano Lett.* **2008**, *8*, 1923−1928.
(41) Zheng, P.; Cushing, S. K.; Suri, S.; Wu, N. Tailoring plasmonic properties of gold nanohole arrays for surface-enhanced Raman scattering. *Phys. Chem. Chem. Phys.* **2015**, DOI: 10.1039/C4CP05291A.
(42) Palik, E. D. *Handbook of Optical Constants of Solids*; Academic Press: New York, 1985.
(43) Thio, T.; Ghaemi, H. F.; Lezec, H. J.; Wolff, P. A.; Ebbesen, T. W. Surface-plasmon-enhanced transmission through hole arrays in Cr films. *J. Opt. Soc. Am. B* **1999**, *16*, 1743−1748.
(44) Skadtchenko, B. O.; Aroca, R. Surface-enhanced Raman scattering of p-nitrothiophenol: Molecular vibrations of its silver salt and the surface complex formed on silver islands and colloids. *Spectrochim. Acta A Mol. Biomol. Spectrosc.* **2001**, *57*, 1009−1016.
(45) Marquestaut, N.; Martin, A.; Talaga, D.; Servant, L.; Ravaine, S.; Reculusa, S.; Bassani, D. M.; Gillies, E.; Lagugné-Labarthet, F. Raman enhancement of azobenzene monolayers on substrates prepared by Langmuir−Blodgett deposition and electron-beam lithography techniques. *Langmuir* **2008**, *24*, 11313−11321.
(46) Schatz, G. C.; Young, M. A.; Van Duyne, R. P. In Surface-enhanced Raman scattering; Kneipp, K., Moskovits, M.,Kneipp, H., Eds.; Springer-Verlag: Berlin, 2006; Vol. *103*, pp 19−46.
(47) Félidj, N.; Truong, S. L.; Aubard, J.; Lévi, G.; Krenn, J. R.; Hohenau, A.; Leitner, A.; Aussenegg, F. R. Gold particle interaction in regular arrays probed by surface enhanced Raman scattering. *J. Chem. Phys.* **2004**, *120*, 7141−7146.
(48) Félidj, N.; Aubard, J.; Lévi, G.; Krenn, J. R.; Salerno, M.; Schider, G.; Lamprecht, B.; Leitner, A.; Aussenegg, F. R. Controlling the optical response of regular arrays of gold particles for surface-enhanced Raman scattering. *Phys. Rev. B* **2002**, *65*, 075419.

DOI: 10.1021/acsphotonics.5b00104
ACS Photonics 2015, 2, 752−759